www.lajss.org
Latin American Journal of Solids and Structures 4 (2007) 149–176

Finite element implementation of an orthotropic plasticity model for sheet metal forming simulations

Luciano P. Moreira[1,*] and Gérard Ferron[2]

[1]Programa de Pós-graduação em Engenharia Metalúrgica, Universidade Federal Fluminense, Volta Redonda, RJ – Brazil
[2]Laboratoire de Physique et Mécanique des Matériaux, Université Paul-Verlaine Metz – France

Abstract

In this work, the implementation procedures for the user Fortran subroutines of the commercial finite element code ABAQUS are described for the particular case of linear elasticity and a plasticity model proposed within the context of the plastic flow theory along with the isotropic work-hardening assumption. The general 3D case is firstly presented and detailed for the implicit and explicit integration techniques available in the ABAQUS code. Afterwards, the equations for the particular plane-stress state are outlined. The corresponding procedures are applied to a plane-stress orthotropic plasticity model. Finally, the implemented user subroutines are validated by means of numerical simulations of sheet metal forming experiments, namely, the hemispherical punch stretching and cup-drawing. The comparisons of the predicted either radial strains or earing formation with the measured data obtained for an IF steel and a tinplate food-can shows the pertinent conditioning of the user subroutines as well as the importance of an accurate description of the range of stresses states involved in sheet metal forming processes.

Keywords: orthotropic plasticity, sheet metal forming, finite element modeling

1 Introduction

Sheet metal forming is an important manufacturing process widely used to produce complex stamped parts starting from flat blank sheets in many sectors such as the automotive, food and beverage cans industries. Due to the global economic context, these sectors are urged to be extremely competitive by decreasing production costs and increasing the process efficiency. The numerical simulation combined with the sheet metal forming skill represents one of the technological innovations available to achieve these requirements since this may drastically decrease the cost of the time consuming traditional tryout steps. In the last 20 years, considerable efforts have been made to improve the finite element method (FEM) based upon incremental or one-step techniques for solving nonlinear problems arising from material behavior, geometry

*Corresp. author email: luciano.moreira@metal.eeimvr.uff.br Received 29 Nov 06; In revised form 7 Mar 07

and friction. Moreover, user-friendly graphical interfaces together with the increasing computer capacity also promoted the numerical simulation to analyze the sheet metal forming process at an industrial scale. In view of these advances, the questions arising from the accuracy or the limitations related to the type of material description adopted to model the sheet behavior became particularly important. From this standpoint, a phenomenological approach is generally favored owing to its straightforward implementation in finite element codes and low computational costs in comparison to physically motivated models based upon the polycrystalline plasticity theories [1, 4].

The present work aims at presenting the procedures used together with the Fortran user material subroutines available in the commercial ABAQUS finite element code. Firstly, the elastic-plastic constitutive equations are outlined for the linear isotropic Hooke's law and the associated plastic flow theory under the isotropic work-hardening assumption. Afterwards, the phenomenological plasticity description proposed by Ferron et al. [8], herefater Ferron's model, is briefly recalled in order to explain the methods used to determine the coefficients defining the initial material anisotropy. The equations needed for the finite element implementation of Ferron's model are then presented for the plane-stress and the 3D generalized stress states. Finally, the numerical predictions obtained with Ferron's model are compared to the measured data determined from the hemispherical punch stretching and the cup-drawing experiments. The discussions are focused on the influence of the yield surface shape in the stress range of interest upon the strain distributions and the final geometry predicted for these sheet metal forming experiments.

2 Elastic-plastic constitutive equations

First of all, the elastic behavior is described by the Hooke's linear elasticity law defined by:

$$\dot{\boldsymbol{\sigma}} = \mathbf{C}^e \colon \dot{\boldsymbol{\epsilon}}^e \tag{1}$$

where $\mathbf{C}^e$ is the 4^{th}order elasticity tensor. By considering the small elastic strains assumption, the elastic-plastic behavior can then be described by the additive decomposition of the total Cauchy strain-rate tensor into an elastic part and a plastic part, that is,

$$\dot{\boldsymbol{\epsilon}} = \dot{\boldsymbol{\epsilon}}^e + \dot{\boldsymbol{\epsilon}}^p \tag{2}$$

in which the plastic strain-rate tensor is determined from the associated plastic flow rule or the normality law defined by:

$$\dot{\boldsymbol{\epsilon}}^p = \dot{\lambda} \frac{\partial f}{\partial \boldsymbol{\sigma}} \tag{3}$$

where $\boldsymbol{\sigma}$ is the Cauchy stress tensor and $\dot{\lambda}$ is the plastic multiplier.

In Eq. (3), f is the yield function which can be defined under the isotropic work-hardening assumption by:

$$f = F(\boldsymbol{\sigma}) - \bar{\sigma} \tag{4}$$

where $F(\boldsymbol{\sigma})$ is a first degree homogeneous stress function and $\bar{\sigma}$ is a scalar measure of the effective stress. The plastic multiplier $\dot{\lambda}$ in Eq. (3) is obtained from the elastic-plastic loading condition, $f = 0$, by applying first the Euler's identity to the yield function, Eq. (4),

$$F(\boldsymbol{\sigma}) = \bar{\sigma} = \boldsymbol{\sigma}\frac{\partial f}{\partial \boldsymbol{\sigma}} \tag{5}$$

and then by calculating the associated plastic work per unit volume from the equivalent plastic work principle, i.e.,

$$\boldsymbol{\sigma} : \dot{\boldsymbol{\epsilon}}^p = \bar{\sigma}\dot{\bar{\epsilon}}^p \tag{6}$$

together with the normality law, Eq. (3), results that the plastic multiplier $\dot{\lambda}$ is equal to the effective plastic strain-rate $\dot{\bar{\epsilon}}^p$ conjugated of the effective stress $\bar{\sigma}$.

The elastic-plastic behavior description is completed by defining the work-hardening evolution with respect to the plastic strain which relates the effective stress-rate to the effective plastic strain-rate as:

$$\dot{\bar{\sigma}} = H(\bar{\sigma})\dot{\bar{\epsilon}}^p \tag{7}$$

where $H(\bar{\sigma}) = d\bar{\sigma}/d\bar{\epsilon}^p$ is the work-hardening rate.

3 General integration method

The ABAQUS FE code provides at the beginning of the time step, for each element integration point, the stress tensor components, σ_{ij}, the increments of the total strain tensor, $\Delta\epsilon_{ij}$, and all the internal or user defined state variables. Bearing in mind deformation-driven problems, as in displacement based and mixed finite element formulations, the stress state at the end of the time step in then obtained from the strain history by means of an integration of the rate constitutive equations in an incremental procedure The general integration procedure is based upon the elastic predictor-plastic corrector method commonly known as the return mapping algorithm. Thus, in order to abridge the notation, let us denote ξ^t as the current value of all variables at the beginning of the time step, ξ^{Trial} as the quantities referring to the elastic prediction and $\xi^{t+\Delta t}$ as the corrected values determined at the end of the time step.

The trial stress components are computed from an elastic prediction by making use of the Hooke's law, Eq. (1), with the total strain increments $\Delta\epsilon_{kl}$, that is,

$$\sigma_{ij}^{Trial} = \sigma_{ij}^t + C_{ijkl}^e \Delta\epsilon_{kl} \tag{8}$$

where for the isotropy case the elasticity tensor C_{ijkl}^e is defined by:

$$C_{ijkl}^e = \lambda\delta_{ij}\delta_{kl} + \mu\left(\delta_{ik}\delta_{jl} + \delta_{il}\delta_{jk}\right) \tag{9}$$

where λ and μ are the Lamè's coefficients. On the other hand, elastic-plastic loading may occur during the current time step if the yield condition is violated by the trial state of stress, that is to say, if the following condition is verified:

$$F(\sigma_{ij}^{Trial}) - \bar{\sigma} \geq 0 \tag{10}$$

Then, the new state of stress is obtained from the plastic correction of the trial state of stress according to the implicit and explicit integration techniques available in the ABAQUS finite element code. In the following, the procedures used together with the Fortran user subroutines UMAT (ABAQUS/Standard) and VUMAT (ABAQUS/Explicit) are presented in details for the general 3D and the plane-stress cases.

3.1 Implicit procedure

The integration procedure used in the ABAQUS/Standard code is based upon the implicit backward Euler scheme where it is firstly necessary to obtain the plastic corrections associated to the trial stress state and then to define the elastic-plastic tangent operator.

3.1.1 Plastic corrections

The solution for the plastic corrections is made with the help of the Newton's method. By denoting c(ξ) the correction associated to the variable ξ, the Hooke's law with the additive decomposition of the total strain, Eqs. (1-2), provide a relationship between the corrections of the stress components and the plastic strain increments as:

$$c(\sigma_{ij}) = -C_{ijkl}^{e}\, c(\Delta\epsilon_{kl}^{p}) \tag{11}$$

Also, the effective stress-strain measures, Eq. (7), must be verified leading to:

$$c(\bar{\sigma}) = H(\bar{\sigma})\, c(\Delta\bar{\epsilon}^{p}) + \Delta\bar{\epsilon}^{p}\frac{\partial H(\bar{\sigma})}{\partial\bar{\sigma}}\, c(\bar{\sigma}) \tag{12}$$

or

$$c(\bar{\sigma}) = \hat{H}(\bar{\sigma})\, c(\Delta\bar{\epsilon}^{p}) \tag{13}$$

where

$$\hat{H}(\bar{\sigma}) = \frac{H(\bar{\sigma})}{1 - \dfrac{\partial H(\bar{\sigma})}{\partial\bar{\sigma}}\Delta\bar{\epsilon}^{p}} \tag{14}$$

Then, the elastic-plastic loading condition, $f = 0$ in Eq. (4), is not satisfied until the solution is reached within a given accuracy, that is,

$$F_{,ij}\, c(\sigma_{ij}) - c(\bar{\sigma}) = -f \tag{15}$$

where $F_{,ij} = \partial f(\sigma_{ij})/\partial\sigma_{ij} = \partial F(\sigma_{ij})/\partial\sigma_{ij}$ since it is assumed hereafter that the work-hardening is a function only of the effective plastic strain.

Moreover, the associated plastic flow rule, see Eq.(3), gives the corrections of the plastic strain increments:

$$c(\Delta\epsilon^p_{ij}) - F_{,ij}\, c(\Delta\bar{\epsilon}^p) - \Delta\bar{\epsilon}^p F_{,ijkl}\, c(\sigma_{kl}) = F_{,ij}\, \Delta\bar{\epsilon}^p - \Delta\epsilon^p_{ij} \tag{16}$$

where $F_{,ijkl} = \partial^2 F(\sigma_{ij})/\partial\sigma_{ij}\partial\sigma_{kl}$. Finally, by combining Eqs. (11-15), the following set of Newton's equations are obtained for the corrections upon the plastic strain components:

$$c(\Delta\epsilon^p_{mn})\left[\delta_{im}\delta_{jn} + C^e_{klmn}\left(F_{,ijkl}\,\Delta\bar{\epsilon}^p + F_{,ij}\,F_{,kl}\,/\hat{H}(\bar{\sigma})\right)\right] = F_{,ij}\left(\Delta\bar{\epsilon}^p + f/\hat{H}(\bar{\sigma})\right) - \Delta\epsilon^p_{ij} \tag{17}$$

Once the plastic corrections are determined, the stress state at the end of the time step is computed iteratively by correcting the trial stress state, Eq. (8), until the elastic-plastic loading condition ($f = 0$) is satisfied within a given accuracy. Thus, the plastic corrections for the stress components are:

$$\sigma_{ij}|_N = \sigma_{ij}|_{N-1} - C^e_{ijkl}\, c(\Delta\epsilon^p_{kl})\big|_N \tag{18}$$

where N is the current Newton's iteration.

The work-hardening evolution, Eq. (7), is then updated from the effective plastic strain which is stored as a state variable defined at the end of Newton's iterations as:

$$\bar{\epsilon}^p|_N = \bar{\epsilon}^p|_{N-1} + \Delta\bar{\epsilon}^p|_N \tag{19}$$

where the effective plastic strain increment $\Delta\bar{\epsilon}^p$ is determined by:

$$\Delta\bar{\epsilon}^p|_N = \Delta\bar{\epsilon}^p|_{N-1} + c(\Delta\bar{\epsilon}^p)|_N \tag{20}$$

In Eq. (20), the correction upon the effective plastic strain increment is calculated by the Newton's equation obtained from the equivalent plastic work associated to the $(N-1)$th iteration:

$$c(\Delta\bar{\epsilon}^p) = \left.\frac{\sigma_{ij}\Delta\epsilon^p_{ij} - \bar{\sigma}\Delta\bar{\epsilon}^p}{\bar{\sigma} + H(\bar{\sigma})\Delta\bar{\epsilon}^p}\right|_{N-1} \tag{21}$$

3.1.2 Elastic-plastic tangent operator

The elastic-plastic tangent operator is defined by consistent linearization of the response function resulting from the integration algorithm as proposed by Simo and Taylor [18]. The consistent stiffness matrix is determined by taking variations with respect to the all variables. Firstly, the generalized Hooke's law, Eq. (1), together with the total strain additive decomposition, Eq. (2), provide the variations between the total strain and stress components:

$$\partial\epsilon_{ij} = S^e_{ijkl}\partial\sigma_{ij} + \partial\epsilon^p_{ij} \tag{22}$$

where

$$S^{e}_{ijkl} = -\frac{\nu}{E}\delta_{ij}\delta_{kl} + \frac{1}{4\mu}\left(\delta_{ik}\delta_{kl} + \delta_{il}\delta_{jl}\right) \tag{23}$$

is the elastic compliances tensor in which E is the Young modulus and ν is the Poisson's ratio. Next, the variations in the associated plastic flow rule, Eq. (3), the elastic-plastic loading condition, Eq. (4), and the effective stress-strain relationship, Eq. (7), give respectively:

$$\partial\epsilon^{p}_{ij} = \partial\bar{\epsilon}^{p} F_{,ij} + \Delta\bar{\epsilon}^{p} F_{,ijkl}\,\partial\sigma_{kl} \tag{24}$$

$$F_{,ij}\,\partial\sigma_{ij} - \partial\bar{\sigma} = 0 \tag{25}$$

$$\partial\bar{\sigma} = H(\bar{\sigma})\partial\bar{\epsilon}^{p} \tag{26}$$

By eliminating $\partial\bar{\sigma}$ and $\partial\bar{\epsilon}^{p}$ in Eqs. (25-26) and replacing the resulting expression in Eq. (24):

$$\partial\epsilon^{p}_{ij} = \frac{F_{,ij}\,F_{,kl}}{H(\bar{\sigma})}\partial\sigma_{kl} + \Delta\bar{\epsilon}^{p} F_{,ijkl}\,\partial\sigma_{kl} \tag{27}$$

and then returning in Eq. (22), the following system of equations is obtained:

$$\partial\epsilon_{ij} = \left[\left(F_{,ij}\,F_{,kl}\right) \diagup H(\bar{\sigma}) + \Delta\bar{\epsilon}^{p} F_{,ijkl} + S^{e}_{ijkl}\right]\partial\sigma_{kl} = S^{ep}_{ijkl}\partial\sigma_{kl} \tag{28}$$

where the term in the bracktes defines the elastic-plastic compliances tensor,that is, S^{ep}_{ijkl}. Therefore, the consistent elastic-plastic tangent operator at the end of the time step is given by:

$$J^{t+\Delta t}_{ijkl} = \left(\partial\sigma_{ij}/\partial\epsilon_{kl}\right)^{t+\Delta t} = \left[S^{ep}_{ijkl}\right]^{-1} \tag{29}$$

3.2 Explicit procedure

In the ABAQUS/Explicit code the global equilibrium equations are solved by means of an explicit integration technique based upon the central difference finite scheme, wherein the integration of the constitutive equations is simply obtained from the plastic strain increments once the elastic-plastic loading condition is verified. Thus, the stress state at the end of the time step is determined by means of the plastic strain increments from the correction of the trial stress state, Eq. (8), that is:

$$\sigma^{t+\Delta t}_{ij} = \sigma^{Trial}_{ij} - 2\mu\Delta\epsilon^{p}_{ij} \tag{30}$$

It should be noted that the correction in Eq. (30) is colinear with the plastic strain increment and, hence, the method should be referred to as the *normal return* algorithm. For the particular case of the von Mises yield criterion represented in the deviatoric stress plane, the algorithm is known as the *radial return* [13]. Therefore, since the plastic strain increments are known from the associated plastic flow rule, Eq. (3), the only quantity which needs to be defined so as to determine the values of all variables at the end of the time step is the effective plastic strain increment $\Delta\bar{\epsilon}^{p}$. An appropriate procedure to define the effective plastic strain increment consists

of calculating the increment of the plastic work associated to the time step increment. From Eq. (6), this can be stated as:

$$\sigma_{ij}^{t+\Delta t}\Delta\epsilon_{ij}^{p} = \bar{\sigma}^{t+\Delta t}\Delta\bar{\epsilon}^{p} \tag{31}$$

and then, by using Eqs. (3) and (7), $\Delta\epsilon_{ij}^{p} = \Delta\bar{\epsilon}^{p}F_{,ij}^{Trial}$ and $\bar{\sigma}^{t+\Delta t} = \bar{\sigma}^{t} + H(\bar{\sigma})^{t}\Delta\bar{\epsilon}^{p}$, with Eq. (30):

$$\Delta\bar{\epsilon}^{p} = \frac{(\sigma_{ij}F_{,ij})^{Trial} - \bar{\sigma}^{t}}{H(\bar{\sigma})^{t} + 2\mu\,(F_{,ij}\,F_{,ij})^{Trial}} \tag{32}$$

3.3 Plane-stress case

For the plane-stress state, such as in the case of shell or membranes elements formulations, the strain component normal to the element in-plane local directions (x,y), that is, ε_{zz} , is not defined from the kinematics but by the restriction $\sigma_{zz} = 0$. As a result, the elastic prediction must be carried from the Hooke's law, Eq. (1), written in the plane-stress state together with the in-plane total strain increments ($\Delta\epsilon_{xx}$,$\Delta\epsilon_{yy}$,$\Delta\gamma_{xy}$), that is,

$$\sigma_{xx}^{Trial} = \sigma_{xx}^{Trial} + \frac{E}{(1-\nu^2)}\left[\Delta\epsilon_{xx} + \nu\Delta\epsilon_{yy}\right] \tag{33}$$

$$\sigma_{yy}^{Trial} = \sigma_{yy}^{Trial} + \frac{E}{(1-\nu^2)}\left[\nu\Delta\epsilon_{xx} + \Delta\epsilon_{yy}\right] \tag{34}$$

$$\sigma_{xy}^{Trial} = \sigma_{xy}^{Trial} + \mu\Delta\gamma_{xy} \tag{35}$$

where it should be noted that in the ABAQUS code the shear strains are defined as $\gamma_{ij} = 2\varepsilon_{ij}(i \neq j)$. Likewise, the effective plastic strain increment and the corresponding plastic corrections must be redefined from the plane-stress state according to the integration procedure.

The increment of the total strain in the normal direction is defined from the additive strain decomposition, Eq. (2), that is, $\Delta\epsilon_{zz} = \Delta\epsilon_{zz}^{e} + \Delta\epsilon_{zz}^{p}$, where the elastic part is obtained from Hooke's law, Eq. (1), by:

$$\Delta\epsilon_{zz}^{e} = -\frac{\nu}{E}\left[\left(\sigma_{xx}^{t+\Delta t} - \sigma_{xx}^{t}\right) + \left(\sigma_{yy}^{t+\Delta t} - \sigma_{yy}^{t}\right)\right] \tag{36}$$

whereas the plastic part is calculated from the plastic incompressibility condition together with the normality law, Eq. (3), as:

$$\Delta\epsilon_{zz}^{p} = -\left(\Delta\epsilon_{xx}^{p} + \Delta\epsilon_{yy}^{p}\right) = -(F_{,xx} + F_{,yy})^{t+\Delta t}\,\Delta\bar{\epsilon}^{p} \tag{37}$$

It should be noted that in all equations defined here above, the terms $F_{,ij}\,(i \neq j)$ are calculated from the expressions of the F function, see Eq. (4), taking into account the symmetry of the Cauchy stress tensor, for instance, $F_{,ij} = \partial F/\partial\sigma_{ij} + \partial F/\partial\sigma_{ji} = 2F_{,ij}\ \forall\,(i \neq j)$.

3.4 Finite-strain formulation

In the ABAQUS code, the description of the elastic-plastic behavior in finite strains is given by the additive decomposition of the total strain-rate tensor, (1) $\mathbf{D} = \mathbf{D^e} + \mathbf{D^p}$, the hypoelastic law, (2) $\boldsymbol{\sigma} = \mathbf{C^e} : \mathbf{D^e} = \mathbf{C^e} : (\mathbf{D} - \mathbf{D^p})$ and the associated plastic flow rule, (3) $\mathbf{D^p} = \dot{\bar{\epsilon}}^p F_{,ij}\, \mathbf{e_i} \otimes \mathbf{e_j}$. These constitutive equations are expressed in a corotational frame defined by an orthonormal basis $\mathbf{e_i}\,(\mathbf{i} = \mathbf{1}, \mathbf{2}, \mathbf{3})$ [17]. The strains components are then obtained by integration of the strain rate components defined in this corotational frame which rotates according to the spin rate [9]. In the ABAQUS input keywords file (*jobname.inp*), the corotational frame is activated with the $*ORIENTATION$ option [17]. Thus, the implementation of the constitutive equations for any orthotropic plasticity model together with the ABAQUS user material subroutines is performed directly since the rotation of the symmetry material axes are taken into account by the corotational frame.

4 Ferron's plasticity model

Phenomenological anisotropic yield criteria are usually defined in the axes of material orthotropic symmetry (x, y, z). In a rolled metal sheet, these axes are parallel to the rolling direction $(x \equiv RD)$, the in-plane transverse $(y \equiv TD)$ and the normal $(z \equiv ND)$ directions respectively. For the particular plane-stress case, the yield function defined by Eq. (4) can be written as:

$$f = F\left(\sigma_{xx}, \sigma_{yy}, \sigma_{xy}\right) - \bar{\sigma} \tag{38}$$

The yield function in Eq. (38) can be rewritten using the principal stress components (σ_1, σ_2) and the orientation between the principal stress axes$(1, 2)$ and the in-plane orthotropy directions (x, y) , i.e., $\alpha \equiv (x, 1) \equiv (y, 2)$ as:

$$f = \phi\left(\sigma_1, \sigma_2, \alpha\right) - \bar{\sigma} \tag{39}$$

Likewise, by introducing a change of variables given by $x_1 = (\sigma_1 + \sigma_2)/2$ and $x_2 = (\sigma_1 - \sigma_2)/2$, where x_1 and x_2 define the centre and the radius of the Mohr's stress circle respectively, the plane-stress yield function can be cast as:

$$f = \psi\left(x_1, x_2, \alpha\right) - \bar{\sigma} \tag{40}$$

Also, the variables x_1 and x_2 can be described in polar coordinates by:

$$x_1 = G\left(\theta, \alpha, \bar{\sigma}\right)\cos\theta \tag{41}$$

$$x_2 = G\left(\theta, \alpha, \bar{\sigma}\right)\sin\theta \tag{42}$$

where $G\left(\theta, \alpha, \bar{\sigma}\right)$ is the polar radius defining a point on the yield locus whereas the polar angle θ defines the current plane-stress state. According to the isotropic work-hardening assumption

it is possible to redefine the polar radius as:

$$G(\theta, \alpha, \bar{\sigma}) = \bar{\sigma} g(\theta, \alpha) \tag{43}$$

where $g(\theta, \alpha)$ is radius normalized by the effective stress $\bar{\sigma}$. Figure 1 illustrates this description in the principal stress space as a function of the orientation angle α where the yield loci are normalized by the effective stress $\bar{\sigma}$ which, in turn, is chosen as the equibiaxial yield stress, that is, $\sigma_b = \sigma_1 = \sigma_2$.

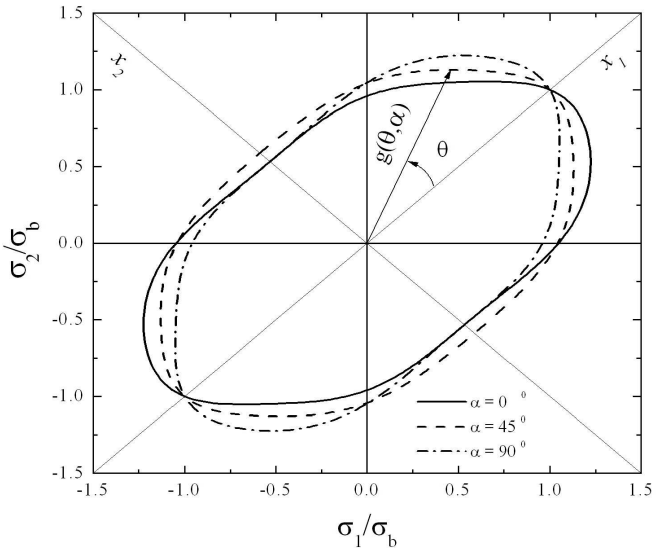

Figure 1: Yield loci of Ferron's plasticity model plotted in the principal stress space (σ_1, σ_2) normalized by the equibiaxial yield stress σ_b as a function of the orientation angle α between the principal stress axes and the in-plane orthotropy directions.

The function $g(\theta, \alpha)$, fullfilling a certain number of consistence conditions vis-à-vis of the orthotropic symmetry, is defined as an extension of a normal anisotropy yield function $g(\theta)$ [8]:

$$(1-k)^{m/6} g(\theta, \alpha)^{-m} = F(\theta)^{m/6} - 2a \sin\theta \cos^{2n-1}\theta \cos 2\alpha + b \sin^{2p}\theta \cos^{2q} 2\alpha \tag{44}$$

where the exponents m, n, p and q are positive integers whereas a and b are dimensionless parameters describing the initial in-plane sheet material anisotropy. The proposed normal anisotropy yield function $g(\theta)$ is an extension of the Drucker's [7] isotropic yield criterion and is given by:

$$(1-k)\, g(\theta)^{-6} = F(\theta) = \left(\cos^2\theta + A \sin^2\theta\right)^3 - k \cos^2\theta \left(\cos^2\theta - B \sin^2\theta\right)^2 \tag{45}$$

where A and B are positive constants and a positive k-value accounts for a flattening of the yield surface near to the plane-strain tension or compression and pure shear stress states, as observed in the yield loci obtained from polycrystalline models [2].

The parameters A, B and k are determined from the experimental values of (σ_b/σ_{45}), (σ_b/τ_0) and R_{45} where τ_0 is the shear yield stress allong the rolling direction whereas σ_{45} and R_{45} are the uniaxial tensile yield stress and the Lankford plastic strain-ratio at 45^0 with respect to the rolling direction respectivelly. The recommended values for the exponents are $m = 2$, $n = 1$ or 2, $p = 1$ or 2 and $q = 1$ or 2, as discussed elsewhere [8]. Then, the parameters a and b can be determined from the R-values obtained at 0^0 and 90^0 from the rolling direction, hereafter, the method R, or from the uniaxial tensile yield or flow stresses (σ_0, σ_{45}, σ_{90}), the method σ, as detailed in [14]. Moreover, Hill's quadratic orthotropic yield criterion [10] can be obtained as a particular case of the Ferron's description by setting in Eq. (44) $k = 0$, $m = 2$ and $n = p = q = 1$.

For finite element implementation purposes, it is more useful to write the Ferron's model with the help of Eq. (37), which for the elastic-plastic loading condition can be rewritten as:

$$\psi\left(\bar{x}_1, \bar{x}_2, \alpha\right) = 1 \tag{46}$$

where $\bar{x}_1 = x_1/\bar{\sigma}$ and $\bar{x}_2 = x_2/\bar{\sigma}$. Then, the effective stress for the Ferron's model is achieved by expressing Eq. (46) together with the Eqs. (41-45):

$$\psi\left(x_1, x_2, \alpha\right) = \left\{ \left[\frac{\left(x_1^2 + Ax_2^2\right)^3 - kx_1^2\left(x_1^2 - Bx_2^2\right)^2}{1-k} \right]^{m/6} - C\cos 2\alpha + D\cos^{2q} 2\alpha \right\}^{1/m} \tag{47}$$

where $C = \dfrac{2a}{(1-k)^{m/6}} \dfrac{x_2 x_1^{2n-1}}{\left(x_1^2 + x_2^2\right)^{n-m/2}}$ and $D = \dfrac{b}{(1-k)^{m/6}} \dfrac{x_2^{2p}}{\left(x_1^2 + x_2^2\right)^{p-m/2}}$.

On the other hand, the partial derivatives of the function $F(\boldsymbol{\sigma})$, see Eq. (4), are obtained from the consistency condition of the yield function cast in the form of Eq. (40), that is, $df = 0$:

$$df = \frac{\partial \psi}{\partial x_1} dx_1 + \frac{\partial \psi}{\partial x_2} dx_2 + \frac{\partial \psi}{\partial \alpha} d\alpha - d\bar{\sigma} = 0 \tag{48}$$

by first calculating dx_1, dx_2 and $d\alpha$ from Eqs. (49-51) as a function of $d\sigma_{xx}$, $d\sigma_{yy}$ and $d\sigma_{xy}$,

$$x_1 = \frac{\sigma_1 + \sigma_2}{2} = \frac{\sigma_{xx} + \sigma_{yy}}{2} \tag{49}$$

$$x_2 = \frac{\sigma_1 - \sigma_2}{2} = \left[\sqrt{\left(\frac{\sigma_{xx} - \sigma_{yy}}{2} \right)^2 + \sigma_{xy}^2} \right] sign\left(\sigma_{xy}\right) \tag{50}$$

$$\tan 2\alpha = \frac{2\sigma_{xy}}{(\sigma_{xx} - \sigma_{yy})} \tag{51}$$

and then returning to Eq. (48), one obtains:

$$F_{,xx} = \frac{1}{2}\left[\frac{\partial \psi}{\partial x_1} + \cos 2\alpha \frac{\partial \psi}{\partial x_2} - \frac{\sin 2\alpha}{2x_2} \frac{\partial \psi}{\partial \alpha} \right] \tag{52}$$

$$F_{,yy} = \frac{1}{2}\left[\frac{\partial\psi}{\partial x_1} - \cos 2\alpha \frac{\partial\psi}{\partial x_2} + \frac{\sin 2\alpha}{2x_2}\frac{\partial\psi}{\partial\alpha}\right] \tag{53}$$

$$F_{,xy} = \frac{1}{2}\left[2\sin 2\alpha \frac{\partial\psi}{\partial x_2} + \frac{\cos 2\alpha}{x_2}\frac{\partial\psi}{\partial\alpha}\right] \tag{54}$$

where $\sin 2\alpha = \sigma_{xy}/2$ and $\cos 2\alpha = (\sigma_{xx} - \sigma_{yy})/(2x_2)$. Likewise, the normal component is obtained from the plastic incompressibility condition together with the associated plastic flow rule, Eq.(3), that is, $F_{,zz} = -(F_{,xx} + F_{,yy})$. Once the first derivatives of the function $F(\sigma)$ are known as a function of the variables x_1, x_2 and α, the definition of the partial derivatives in the form $F_{,ijkl}$, see Eq. (16), is straightforward.

The extension to the 3D general case is done assuming firstly that the plastic flow is independent of the hydrostatic pressure. Then, the effect of the normal stress component σ_{zz} is accounted for by replacing σ_{xx} and σ_{yy} in the plane-stress description by $(\sigma_{xx} - \sigma_{zz})$ and $(\sigma_{yy} - \sigma_{zz})$ respectively. Next, the effects of the through-thickness shear stress components $(\sigma_{xz}, \sigma_{yz})$ are considered by means of quadratic terms. Finally, the proposed 3D version of the Ferron's model is given by:

$$f = \Phi(x_1, x_2, \alpha, \sigma_{xz}, \sigma_{yz}) - \bar{\sigma} = \sqrt{\psi^2(x_1, x_2, \alpha) + \beta\sigma_{xz}^2 + \gamma\sigma_{yz}^2} - \bar{\sigma} \tag{55}$$

where $\beta = \gamma = 3$ in the same way as for the von Mises isotropic yield criterion and $\psi(x_1, x_2, \alpha)$ is the Ferron's yield function for the plane-stress state defined by Eq. (45). The partial derivatives of the 3D Ferron's yield function, required for the calculation of the plastic strain increments corrections and the elastic-plastic tangent operator, are obtained in the same way as for the plane-stress case.

5 Numerical simulations

In all the numerical simulations discussed hereafter, the effective plastic stress-strain relationship is defined by the Swift-Krupkwoski power law:

$$\bar{\sigma} = K(\epsilon_0 + \bar{\epsilon}^p)^N \tag{56}$$

where K, ϵ_0 and N are the strength coefficient, the pre-strain and the strain-hardening exponent respectively. In all cases, the elastic constants are taken equal to $E = 200,000$ MPa and $\nu = 0.29$. Moreover, the contact between the blank and the tooling is described by the Coulomb friction law. The simulations were performed with a workstation HP-UX 9000/785 J5600 model with 1.5 Gb RAM. For consistency, all the predictions related to the Hill's quadratic yield criterion discussed herefater have been obtained as a particular case of the Ferron's model unless othewise stated.

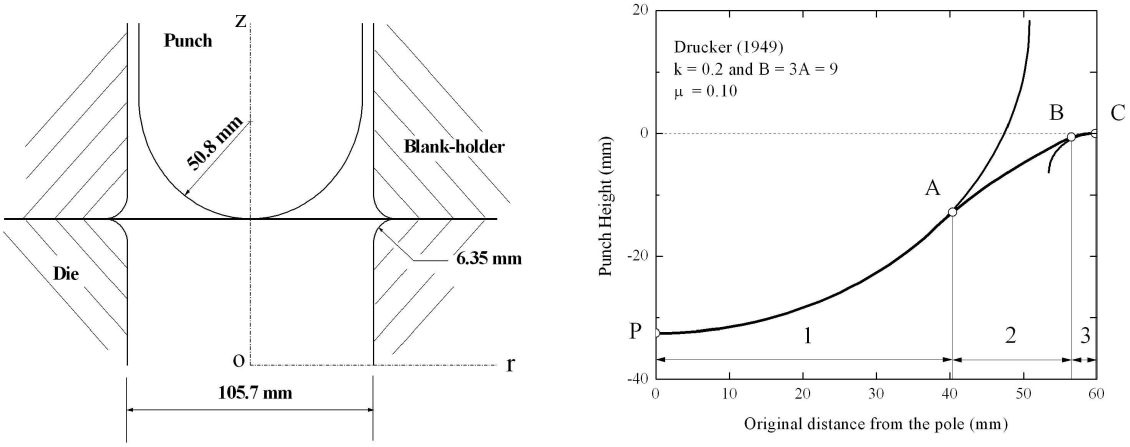

Figure 2: Hemispherical punch stretching experiment for metal sheets: (a) schematic view with standard dimensions and (b) characteristical regions of a deformed blank.

5.1 Hemispherical punch stretching

Figure 2(a) shows schematically the geometry adopted in the simulations of the hemispherical punch stretching experiment, which is the same as in the experimental and numerical work conducted by Knibloe and Wagoner [12]. Owing to the axial symmetry and assuming a normal anisotropy behavior, the analysis is described by an axisymmetric model. The simulations were performed with the implicit code ABAQUS/Standard together with the user material subroutine UMAT. The tooling is described by analytical rigid surfaces whereas the sheet blank by 50 axisymmetric shell elements with 9 thickness integration points, SAX1, as defined in the ABAQUS terminology. On the other hand, the contact is modeled by the option $*CONTACT\,PAIR$, $INTERACTION = ROUGH$ wherein the friction behavior is described by the Coulomb's law. The blank is fully clamped at the edge ($r = 59.2\,mm$) to assure the strectching boundary conditions replacing, in this way, the need for modeling either the lock-bead or the blank-holder.

Figure 2(b) shows the deformed blank obtained for an isotropic material defined with Drucker's yield criterion. From this figure it is possible to distinguish three typical regions of the hemispherical punch strecthing. In the first one, between points P and A, the blank is in contact with the punch. Next, there is a unsupported region located between points A and B. Finally, the blank envelops the die shoulder between the points B and C, which corresponds to the clamped edge. It should be observed that the range of stress states in the hemispherical punch stretching varies from the equibiaxial stretching at the pole ($r = 0$) to the plane-strain tension at the clamped blank edge. Therefore, the ratio between the major principal stress component

in plane-strain tension and the equibiaxial tension yield stresses, namely, $P = \sigma_{PS1}/\sigma_b$, seems to be the appropriate material parameter controlling the strain distributions in the hemispherical punch stretching experiment. A numerical study is firstly presented in order to analyze the effects of the rheological and the tribological parameters upon the numerical predictions of the radial and the hoop strains obtained from the simulations of the hemispherical punch stretching experiment. Then, the experimental data obtained by Knibloe and Wagoner [12] is compared with the numerical predictions determined with Ferron's model.

5.1.1 Numerical study

The blank has an initial thickness of 0.89 mm with the plastic behavior defined in uniaxial tension by $K = 500$ MPa, $\epsilon_0 = 0.002$ and $N = 0.2$ whereas the material anisotropy is described by the yield loci plotted in Fig. 3 as a function of the normal anisotropy parameter R.

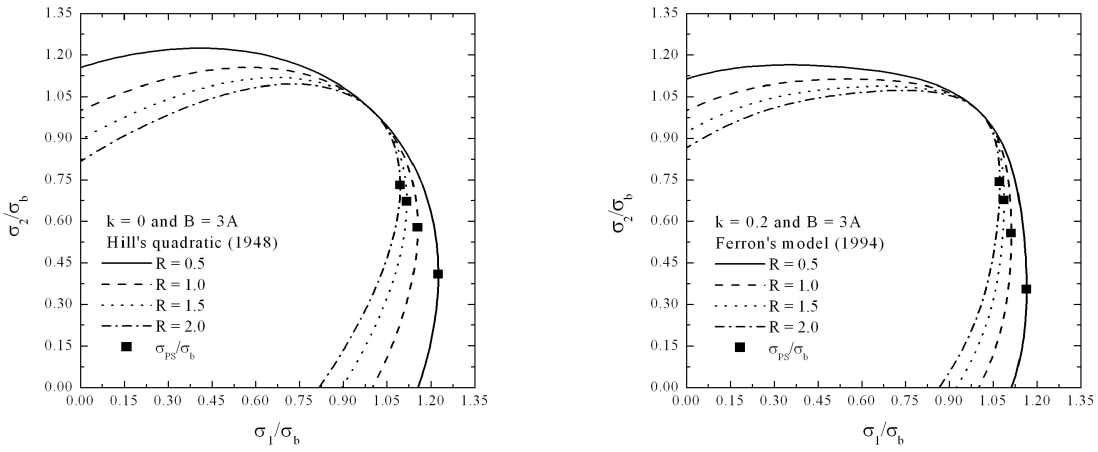

(a) (b)

Figure 3: Yield loci for different values of the normal anisotropy coefficient R determined with: (a) Hill's quadratic yield criterion ($k = 0$) and (b) Ferron's model ($k = 0.2$).

On the other hand, Figs. 4 and 5 shows the corresponding numerical predictions of the radial strains determined for a punch height $PH = 32.5$ mm using a Coulomb's friction coefficient $\mu = 0.10$ between the blank and the tooling. These strain distributions were obtained at the shell mid-surface with respect to the original distance from the pole. In a qualitative way, both yield loci descriptions adopted in the simulations provide the same trends, namely, as the R-value increases the radial strains at the pole decreases while higher stretching is obtained close to the blank clamped edge. These effects are better explained as a function of the material parameter $P = \sigma_{PS1}/\sigma_b$. From Fig. 3 one can observe that the material parameter P decreases

with either the R-value or the k parameter in Eq. (45), i.e., from 0 for Hill's quadratic yield criterion to 0.2 with Ferron's model which, in turn, provides a flattenning of the yield locus near to the plane-strain tension stress state. Consequently, the radial strains at the blank edge are favored, wherein the stress state is plane-strain tension, in detriment to the equibiaxial stretching at the pole. Moreover, the peak strain is located at larger distances from the pole, as shown in Fig. 5(a) for the Ferron's model, since the radial displacements are smaller for decreasing values of the parameter P. On the other hand, the hoop strains distributions are consistent with the equibiaxial stretching at the pole and the plane-strain tension at the clamped edge. Also, the small radial displacements resulting from the higher values of the parameters R and or k, explains the decreasing of the hoop strains for small P-values.

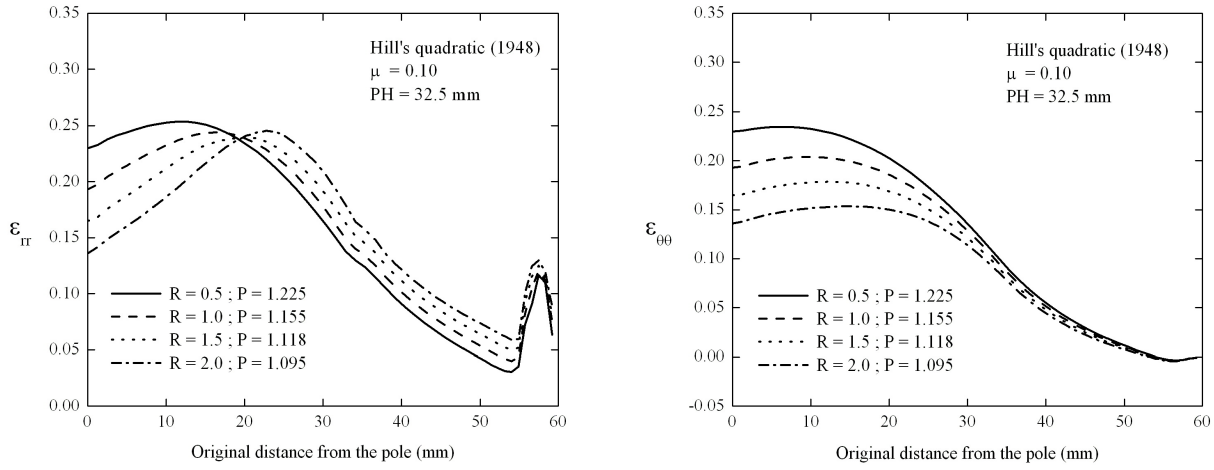

Figure 4: Numerical predictions of the radial (ϵ_{rr}) and the hoop ($\epsilon_{\theta\theta}$) strains distributions obtained for the hemispherical punch stretching with Hill's quadratic yield criterion as a function of the normal anisotropy coefficient R.

Figure 6 shows the influence of the Coulomb's friction coefficient μ upon the strains distributions determined assuming an isotropic material described by the Drucker's yield criterion with $k = 0.2$ and $B = 3A$ in Eq. (45), corresponding to $P = 1.112$. In the contact region between the blank and the punch, increasing the friction coefficient reduces the blank slip and thus either the radial or the hoop strains in the regions near to the pole. For a given punch height, the radial peak strain starts prematurely and is shifted away from the pole as the μ-value is increased. In the unsupported region, the radial strains increase with the friction coefficient whereas the hoop strains are slightly affetcted. Conversely, the plane-strain tension observed in the regions situated along the die arc and near to the clamped independs of the friction behavior.

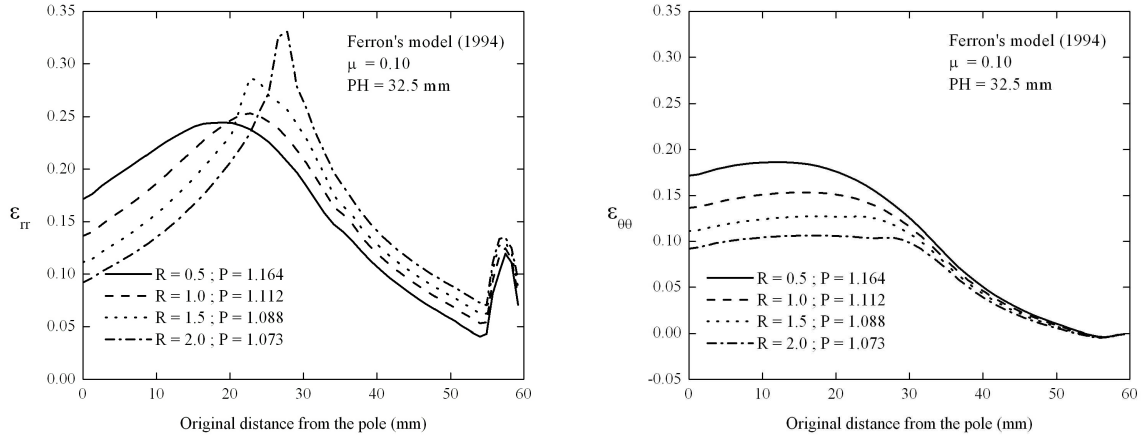

Figure 5: Numerical predictions of the radial (ϵ_{rr}) and the hoop ($\epsilon_{\theta\theta}$) strains distributions obtained for the hemispherical punch stretching with Ferron's model as a function of the normal anisotropy coefficient R.

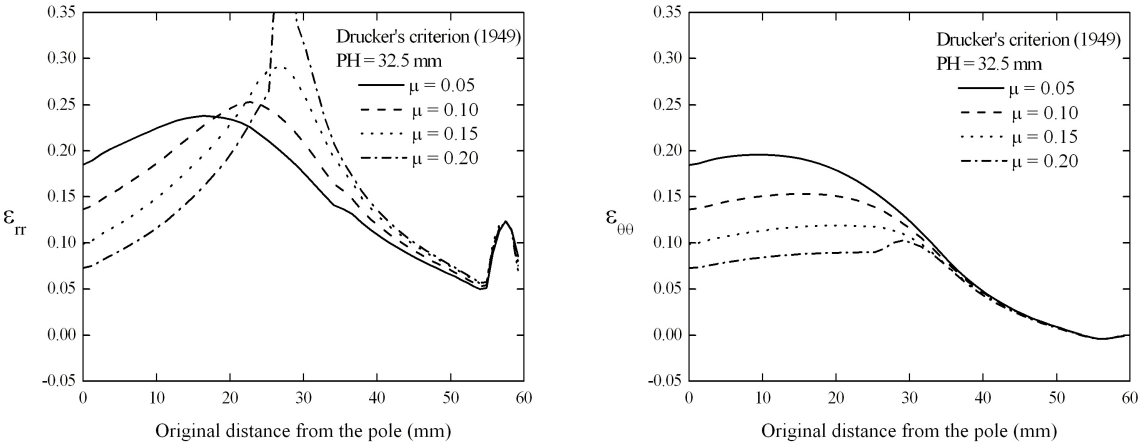

Figure 6: Numerical predictions of the radial (ϵ_{rr}) and the hoop ($\epsilon_{\theta\theta}$) strains distributions obtained for the hemispherical punch stretching with Drucker's yield criterion as a function of the Coulomb's friction coefficient μ.

At this point, it is interesting to resume the role of either the rheological or tribological parameters upon the strains predictions of the hemispherical punch stretching experiment. From the sheet metal formability standpoint, the preponderant material parameters upon the limiting strains are the hardening exponent N, the strain-rate sensitivity M and the normal anisotropy coefficient or the Lankford value R. For a given tooling geometry, the limiting strains are also influenced by the temperature, the initial blank thickness and the tribology condition between the blank and the tooling surfaces. From the parametric study conducted by Burford et al. [6] for the full-dome hemispherical punch strecthing test, the parameters controlling the critical dome height at the pole can be classified in a decreasing order of importance as μ, N, R and M. On the other hand, the numerical study performed in the present work points out, for a given work and strain-rate hardening descriptions, that the strains resulting from the hemispherical punch strecthing and, as a consequence, the critical dome height at the pole as a function of either the material anisotropy or the friction behavior, may be better explained from the stress-ratio $P = \sigma_{PS1}/\sigma_b$ in preference to the traditional R-value. Actually, the effects of higher μ-values are, in a qualitative way, the same as those caused by decreasing P-values. This coupling effect between the rheological and tribological parameters is better illustrated in Fig. 7 where the strain-paths, determined at an original distance from the pole equal to 27.2 mm, are plotted as a function of the parameters P and μ. The peak-strain leading to the strain localization, characterized by an abrupt change in the strain-path towards the plane-strain state, can be ascribed to the effects of either the material or the tribological parameters P and μ respectively.

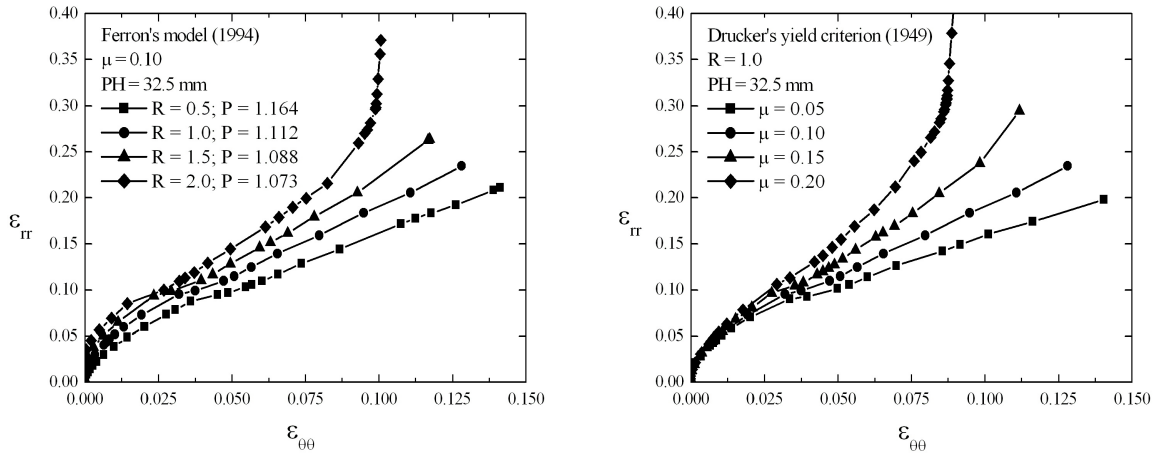

Figure 7: Strain-paths $(\epsilon_{rr}, \epsilon_{\theta\theta})$ determined for an element located at 27.2 mm from the original distance of the pole as a function of (a) the rheological and (b) the tribological parameters.

5.1.2 Comparisons with experimental data

In the work of Knibloe and Wagoner [12], an aluminum killed steel with an initial thickness of 1.04 mm is tested under dry conditions. The material behavior of this steel is described in uniaxial tension by $K = 598$ MPa, $\epsilon_0 = 0.0023$ and $N = 0.23$. Knibloe and Wagoner [12] have also performed FEM simulations with the Hill's quadratic and non-quadratic [11] yield criteria, the later defined as:

$$|\sigma_1 + \sigma_2|^m + (1 + 2R)\,|\sigma_1 - \sigma_2|^m = (1 + R)\,\bar{\sigma}^m \tag{57}$$

where m is a positive exponent which can be obtained to fit the uniaxial and plane-strain tension data [15]. In the present numerical simulations, the parameters A, B and k defining the normal plastic anisotropy in Ferron's model, see Eq. (45), have been identified so as to respect the ratio of the flow stresses determined by Eq. (57) with $m = 2.38$ between the major principal plane-strain tension, σ_{PS1}, and the uniaxial tension, σ_u, together with the experimental normal anisotropy coefficient $R = 1.48$. Table 1 compares the stresses-ratios determined for the aluminum killed steel with Ferron's model and Hill's quadratic and non-quadratic yield criteria where one can observe that the smallest $P = \sigma_{PS1}/\sigma_b$ value is obtained by Ferron's model with $A = 3.65$, $B = 12.23$ and $k = 0.148$. The corresponding strains distributions obtained from the numerical simulation of the hemispherical punch stretching together with Ferron's model are compared in Fig. 8 to the experimental data measured by Knibloe and Wagoner [12]. The numerical predictions determined by Ferron's model with a friction coefficient $\mu = 0.20$ are in good agreement with the experimental values whereas Knibloe and Wagoner [12] have adopted $\mu = 0.268$ and 0.639 for the Hill's quadratic and non-quadratic yield criteria respectively. Clearly, this unreasonable μ-value is due to the high value of the parameter $P = \sigma_{PS1}/\sigma_b$ predicted by the Hill's non-quadratic yield criterion, as indicated in Table 1.

Table 1: Stress-ratios for the aluminun killed steel analyzed by Knibloe and Wagoner [12].

Yield criterion	σ_b/τ	σ_b/σ_u	σ_{PS1}/σ_b	σ_{PS2}/σ_b	σ_{PS1}/σ_u	σ_{PS2}/σ_u
Hill's quadratic	1.190	1.113	1.119	0.668	1.246	0.744
Hill's non-quadratic	1.783	0.980	1.200	0.553	1.176	0.542
Ferron's model	1.962	1.070	1.099	0.642	1.176	0.687

5.2 Cup-drawing experiments

In this section the earing profile determined for an IF steel is firstly compared to the numerical predictions obtained from Hill's quadratic yield criterion and Ferron's model by using either shell and linear solid elements to mesh the blank. Then, the earing formation obtained for a

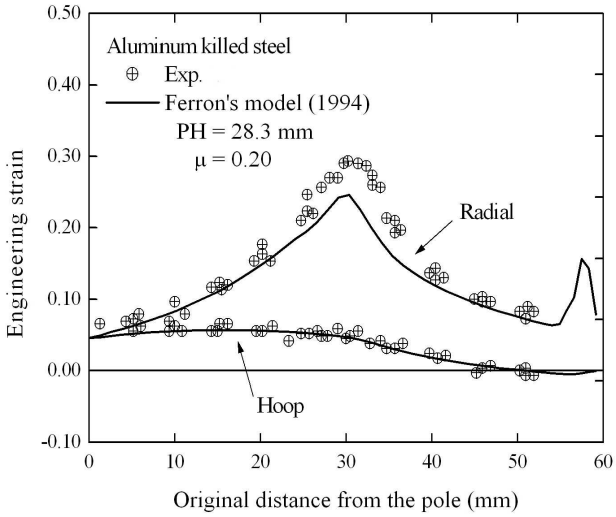

Figure 8: Comparison between the numerical predictions determined with Ferron's model and the experimental strains distributions obtained from the hemispherical punch stretching by Knibloe and Wagoner [12].

tinplate steel is discussed from the standpoint of the material parameters describing the effects of the in-plane anisotropy commonly observed in the deep-drawing of circular blank sheets.

5.2.1 Cup-drawing of an IF steel

The geometry and the blank mesh used in the simulations of the cup-drawing experiment performed on an IF steel with an initial thickness of 0.7 mm are depicted in Fig. 9. Due to the material orthotropy and the axial symmetry, only one quarter of the cup-drawing geometry is taken into account. The cup-drawing tooling mesh is described by analytical rigid surfaces and 4-node bilinear discrete rigid elements (R3D4) in ABAQUS/Standard and ABAQUS/Explicit codes respectively. The blank is meshed by either 756 quadrangular shell with 5 integration points through the thickness or 1,512 two-layer 3D linear solid elements. Only reduced element integration rule have been tested with both shell (S4R) and solid (C3D8R) elements formulations. In all cases analyzed herefater, the blank-holder force is taken equal to 42.5 kN whereas the Coulomb friction coefficient has been taken equal to $\mu = 0.15$ between the punch and the blank and $\mu = 0.05$ elsewhere.

Table 2 presents the material parameters determined for the IF steel from two uniaxial tensile tests conducted on specimens taken along the parallel (0^0), diagonal (45^0) and transverse (90^0) angular orientations with respect to the sheet rolling direction (RD). In this table, the yield σ_y

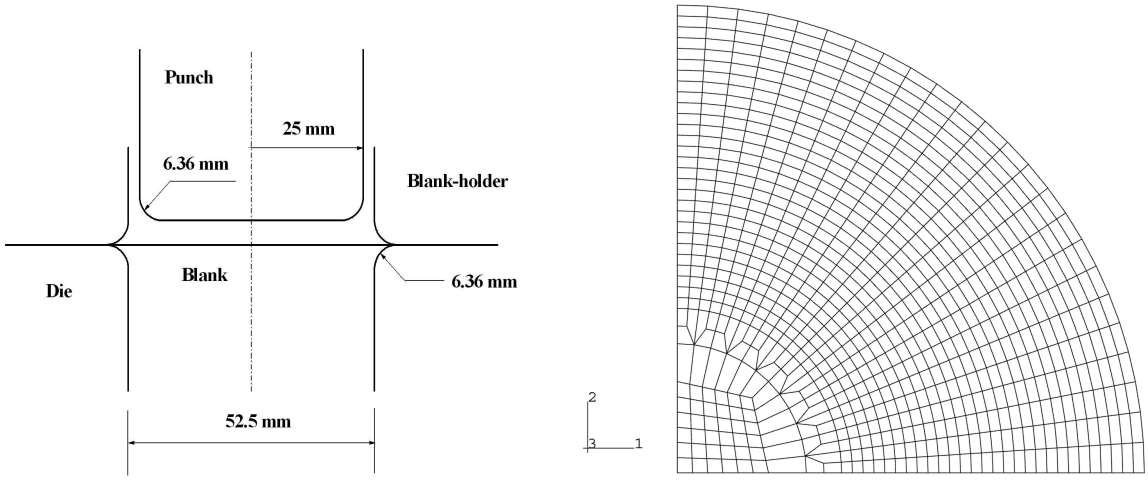

(a) (b)

Figure 9: Numerical simulation of the cup-drawing experiment: (a) tooling dimensions and (b) finite element mesh of the blank.

and the flow σ_f stresses have been determined at 0.2 and 20 % plastic strain levels respectively whereas the plastic anisotropy coefficients R have been defined at 18% of plastic strain. In this case, the choice is made upon the flow stress definition which is more pertinent than the initial yield stress to model the plastic behavior at larger strains when the assumption of isotropic work-hardening is assumed. This IF steel presents a four-ear profile located at 0^0 and 90^0 with respect to the RD with mean cup heights of 45.99 ± 0.11mm at the peaks and 43.97 ± 0.05 mm at the troughs situated near to the diagonal angular orientation [5].

Table 2: Material parameters for the IF steel used in the cup-drawing experiment.

Angle (Degrees)	σ_y(MPa)	K(MPa)	ϵ_0	N	R(18%)	σ_f(MPa)
0	155.0	510	0.0048	0.223	1.884	358.0
45	161.5	523	0.0036	0.209	1.527	375.4
90	153.0	510	0.0038	0.216	2.268	361.4

Provided that only uniaxial tensile data is available, the parameters of Ferron's model were determined by adopting a positive k-value (0.2) and imposing the relationship $B = 3A$. Afterwards, the parameter A is obtained from the experimental R_{45} value. The parameters a and b in Eq. (44) describing the initial material anisotropy, are then determinated by applying the methods R and σ introduced in Section 4. In order to assure a good compromise between

the experimental data and the theoretical predictions for the angular evolutions of the plastic anisotropy coefficient, $R_{(\alpha)}$, and the uniaxial tensile flow stress, $\sigma_{(\alpha)}$, different values of the exponents (n, p) can be considered. In fact, the combinations of interest are $(n = 1, p = 2)$, $(n = 2, p = 1)$ and $(n = 2, p = 2)$, in addition to the pair $(n = 1, p = 1)$ which provides the correlation between R and σ corresponding to the Hill's quadratic yield criterion.

The effects of the method adopted to determine the parameters a and b are illustrated in Fig. 10 as a function the exponents (n, p) together with the experimental values of the normalized uniaxial tensile flow stresses $(\sigma_{45}/\sigma_0, \sigma_{90}/\sigma_0)$ and the plastic anisotropy coefficients (R_0, R_{45}, R_{90}). It is interesting to note that neither of (n, p) pairs provides a good agreement between both $R_{(\alpha)}$ and $\sigma_{(\alpha)}$ angular evolutions. Nevertheless, for a given plastic anisotropy angular evolution, the angular dependence of the uniaxial tensile flow stress is clearly decreased when the exponents (n, p) are equal to 2.

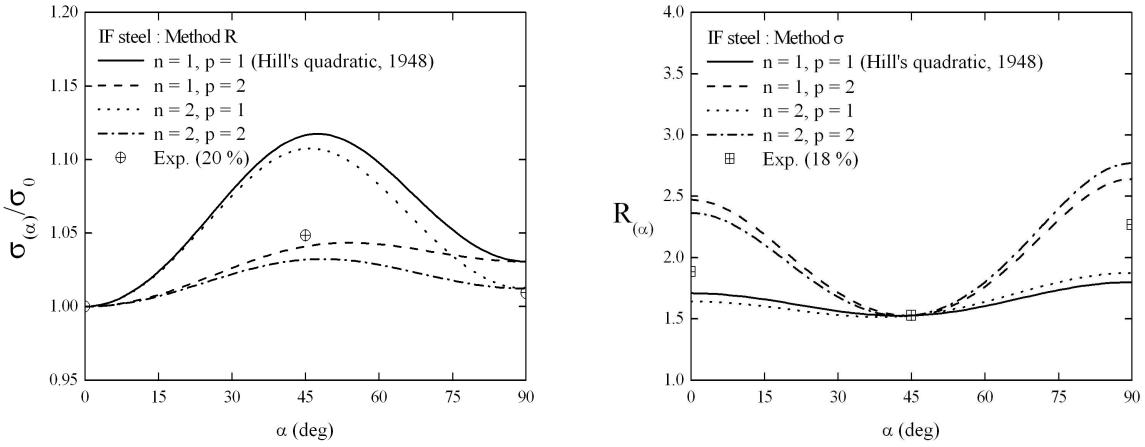

Figure 10: Comparison between the predictions determined with Ferron's model and the experimental data obtained for an IF steel : (a) orientation dependence of the normalised uniaxial tensile flow stress and (b) orientation dependence of the anisotropy coefficient.

Tables 3 compares the number of time increments and the CPU time by adopting reduced integration shell elements to mesh the blank obtained with Ferron's model (method R) and the keyword $*POTENTIAL$, which is used to define the Hill's quadratic yield criterion in the ABAQUS code. Although the CPU times are larger with use of the user subroutines, the implementation of Ferron's model shows a pertinent conditioning since it leads to almost the same number of increments in comparison to the use of the option $*POTENTIAL$ for either the implicit or the explicit integration techniques available in the ABAQUS finite element code. Fig. 11 shows the predicted earing profile percentage determined for an IF steel with Hill's quadratic yield criterion obtained either as a particular case of Ferron's model and by means

of the keyword $*POTENTIAL$. For comparisons purposes, the earing profile percentage is defined as:

$$EP_{\%} = (h_\alpha - h_{min}) / h_{min} \tag{58}$$

where h_α and h_{min} correspond to the cup height at an angular orientation α with respect to the rolling direction and the minimum cup heigth respectively. The results obtained with the user subroutines UMAT (ABAQUS/Standard) and VUMAT (ABAQUS/Explicit) are in good agreement with the earing profile determined with the option $*POTENTIAL$ as well as with experimental trend. Nonetheless, the implicit and explicit integration techniques forecasted quite different ears amplitudes. Actually, this is due to the contact treatement used together with the shell elements in the ABAQUS/Standard wherein the sheet thickness variation is not taken into account when the tooling is represented by analytical rigid surfaces.

Table 3: Number of time increments and CPU time obtained in the numerical simulations of the cup-drawing experiment of an IF steel performed with shell reduced integration elements.

	ABAQUS/Standard		ABAQUS/Explicit	
Yield criterion	Increments	CPU time (s)	Increments	CPU time (s)
*POTENTIAL	1,373	10,897	18,207	502
Ferron's model	1,317	16,418	18,607	859

Fig. 12 compares the earing profile measured for an IF steel with the predictions determined from the numerical simulations performed with the user subroutine VUMAT using reduced integration shell elements. These results are plotted as a function of the method to identify the anisotropy material parameters a and b in Ferron's model. Firstly, the experimental ear height, i.e., $(h_{0,90} - h_{45}) \cong 2$ mm, is overestimated and underestimated when the method R is used together with Hill's quadratic yield criterion and Ferron's model respectively. Likewise, it is worthwhile to note that the orientation dependence of the uniaxial tensile flow stress, $\sigma_{(\alpha)}$, is overpredicted by Hill's quadratic yield criterion and underpredicted by Ferron's model, as shown in Fig. 10(a). Conversely, a better prediction is achieved when the material parameters describing the in-plane anisotropy are adjusted to the experimental $\sigma_{(\alpha)}$ values, in this case by Ferron's model together with $n = 2$ and $p = 2$.

The finite element earing predictions determined with linear solid elements using reduced integration rule are shown in Fig. 13. For the case of the user subroutine UMAT, one can observe a good agreement with the results obtained from the simulations realized with ABAQUS/Explicit using reduced integration shell elements. On the other hand, though the predictions given by VUMAT are qualitatively in agreement with the material descriptions adopted, the ears heights at the angular orientations 0^0 and 90^0 are overestimated. This can be atributed to the excitation of hourglass modes which may produce mesh distortions in reduced integration elements.

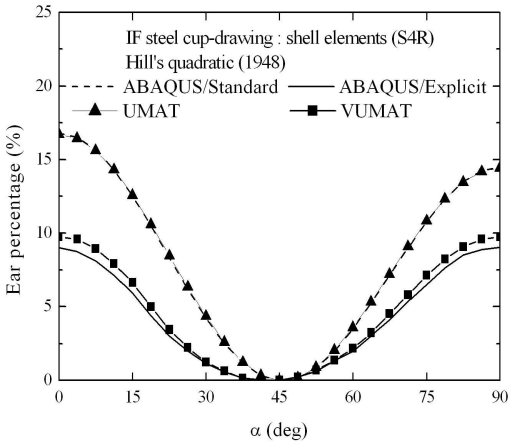

Figure 11: Comparison between the predicted earing profile for an IF steel determined with reduced integration shell elements and Hill's quadratic yield criterion as a function of the finite element integration technique.

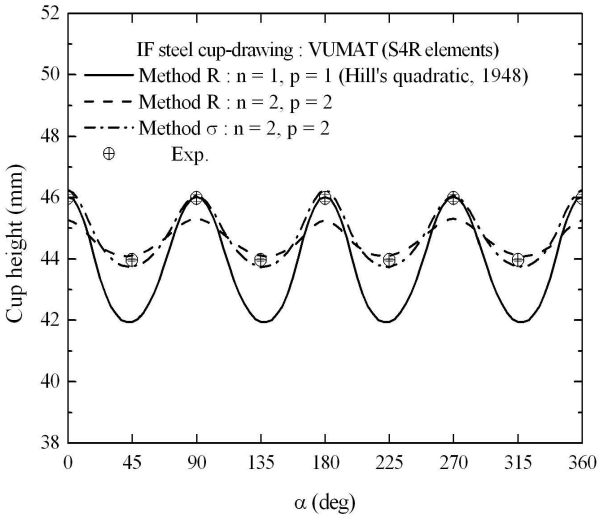

Figure 12: Comparison of the experimental and predicted earing profile for an IF steel determined with reduced integration shell elements as a function of the identification method of the anisotropy parameters in Ferron's model.

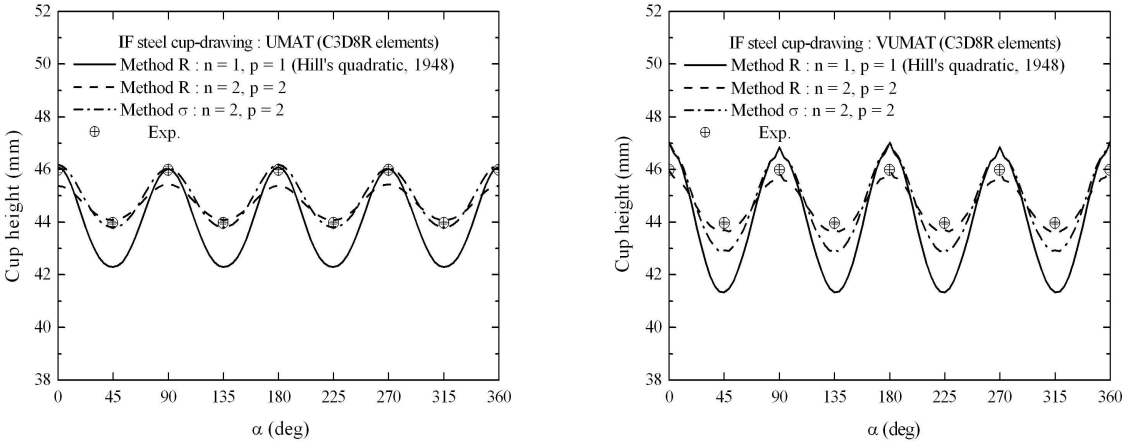

Figure 13: Comparison of the experimental and predicted earing profile for an IF steel determined with linear solid reduced integration elements as a function of the identification method of the anisotropy parameters in Ferron's model: (a) ABAQUS/Standard with UMAT and (b) ABAQUS/Explicit with VUMAT.

5.2.2 Earing formation on a tinplate steel food-can

At this stage, is interesting to discuss the different explanations proposed in the literature concerning the earing formation in the cup-drawing experiment of metal sheets. According to the first one, the ears and respectively the troughs are formed at the angular orientations α corresponding to the maximum and the minimum values of the plastic anisotropy coefficient R [5,10]. This idea is based upon the higher and or lower radial strains obtained from orthoradial compression in the cup flange, namely, at $\alpha + \pi/2$, for larger and lower $R-$values respectively. Another explanation, introduced by Panchanadeeswaran et al. [16], is based on the fact that the stress states encountered at the edge of the flange and the flange cup varies between an uniaxial orthoradial compression to a pure shear. In this case, the ear formation is related to the shearing effects appearing when the compressive orthoradial or hoop stress is not coaxial with the material in-plane orthotropy directions. This off-axis anisotropy effect can be quantified by the parameter $\Gamma_{(\alpha)} = \dot{\epsilon}^p_{12}/\dot{\epsilon}^p_{11}$ proposed by Barlat and Richmond [3], which is defined with Ferron's model as:

$$\Gamma_{(\alpha)} = - \left. \frac{\partial g\left(\theta, \alpha\right)/\partial \alpha}{2g\left(\theta, \alpha\right)} \right|_{\theta=\pi/4} \tag{59}$$

Moreover, since the uniaxial yield stress at the angular orientation α is $\sigma_{(\alpha)} = \sigma_b \sqrt{2}\, g\left(\pi/4, \alpha\right)$,

see Fig. 1, the parameter $\Gamma_{(\alpha)}$ for a fixed effective stress $\bar{\sigma}$ is given by:

$$\Gamma_{(\alpha)} = -\frac{\partial\sigma_{(\alpha)}/\partial\alpha}{2\sigma_{(\alpha)}} \tag{60}$$

where it should be noted that this relationship holds true for any anisotropic yield criterion under the assumption of an isotropic work-hardening.

The two explanations lead to the same qualitative conclusions that the ears develops at 0^0 and 90^0 for materials with a minimum of $R_{(\alpha)}$ and a maximum of $\sigma_{(\alpha)}$ for $0 < \alpha < \pi/2$ and near to 45^0 for materials with a minimum of $\sigma_{(\alpha)}$ or a maximum of $R_{(\alpha)}$. However, as pointed out from the numerical predictions of the cup-drawing for an IF steel, the explanation for earing formation based upon the orientation dependence of the yield and/or flow stress determined in the uniaxial tensile test, $\sigma_{(\alpha)}$, seems to be more quantitatively convincing than the one based on the orientation dependence of the anisotropy coefficient, $R_{(\alpha)}$.

The idea of earing formation based upon the parameter $\Gamma_{(\alpha)}$ has been firstly advanced in the work of Panchanadeeswaran et al. [16] and further discussed by Barlat et al. [10]. Assuming either a plane-stress state or a plane-strain hoop compression at the cup flange, Barlat et al. [10] demostrate that the normalised angular variations of the radial velocity of the rim cup, v_r, and the uniaxial compression yield stress, $\sigma_{(\alpha)}$, are both linked to the parameter $\Gamma_{(\alpha)}$ by:

$$\frac{1}{v_r}\frac{dv_r}{d\alpha} = \frac{1}{\sigma_{(\alpha)}}\frac{d\sigma_{(\alpha)}}{d\alpha} = 2\Gamma_{(\alpha)} \tag{61}$$

Panchanadeeswaran et al. [16] derived a simplified model to assess the normalised radius of the cup flange which is given as:

$$\frac{r_{(\alpha)}}{r_{\alpha_0}} = 1 + \left[\frac{r}{r_{\alpha_0}} - 1\right]\left\{1 - exp\left[2\int_0^{\alpha}\Gamma_{(\alpha+\pi/2)}d\alpha\right]\right\} \tag{62}$$

where it should be noted that the parameter Γ is evaluated at angular orientation $\alpha = \alpha + \pi/2$, i.e., under uniaxial compression whereas r and α_0 are the initial blank radius and the reference ear orientation angle respectively. This model can be solved together with Eq. (61) so as to obtain a normalised amplitude of the cup flange profile as:

$$\frac{\Delta r_{(\alpha)}}{\Delta r_{\alpha_0}} = \frac{r_{(\alpha)} - r}{r_{\alpha_0} - r} = \left.\frac{\Delta\sigma_{(\alpha)}}{\sigma_{(\alpha)}}\right|_{\alpha=\alpha+\pi/2} \tag{63}$$

In the following, the experimental flange profile of the deep-drawing of a tinplate steel food-can [5] is compared to the predictions determined with the help of the simplified model proposed by Panchanadeeswaran et al. [16], as defined by Eq. (63). The food-can is deep-drawn from a tinplate steel with an initial blank radius of 74 mm and 0.24 mm thickness and tooling dimensions given by: punch radius, 41.675 mm, punch nose radius, 1.25 mm, die gap, 42.05 mm, die profile radius, 2 mm. The blank-holder force and the punch displacement are taken equal as 30 kN and

39 mm respectively. The mechanical properties of the tinplate steel determined from uniaxial tensile tests are given in Table 4. Thus, as for the IF steel, the value $k = 0.2$ and the relationship $B = 3A$ have been imposed in Eq. (45) so as to obtain the parameter A from the experimental value of R_{45}. For this material, the orientation dependencies of both $R_{(\alpha)}$ and $\sigma_{(\alpha)}$ are quite well described by using the method R together with the exponents $n = p = 2$, as shown in Fig. 14. Figure 15 shows the predicted tinplate steel food-can determined with Hill's quadratic yield criterion, where a 3D geometry showing the complete flange profile has been adopted for illustration purposes. Figure 16(a) compares the averaged experimental flange profile of the tinplate steel food-can and the calculated results given by the simplified model, see Eq. (63), with Hill's yield criterion and Ferron's model. A good agreement is achieved with Ferron's model since this description provides a small angular variation of either the uniaxial tensile yield stress , $\sigma_{(\alpha)}$, and hence of the parameter $\Gamma_{(\alpha)}$, as shown in Fig. 16(b).

Table 4: Material parameters of the tinplate steel food-can.

Angle (Degrees)	σ_y(MPa)	K(MPa)	ϵ_0	N	R(18%)
0	352	668	0.023	0.167	0.670
45	347	656	0.021	0.164	1.017
90	349	665	0.017	0.159	0.858

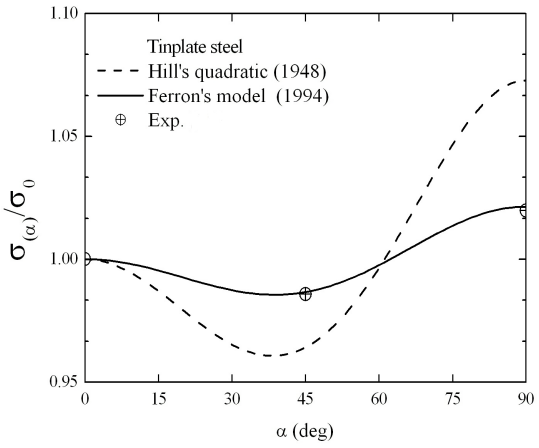

Figure 14: Comparison between the experimental normalised uniaxial tensile yield stress of the tinplate steel and the predictions determined with Hill's quadratic yield criterion and Ferron's model.

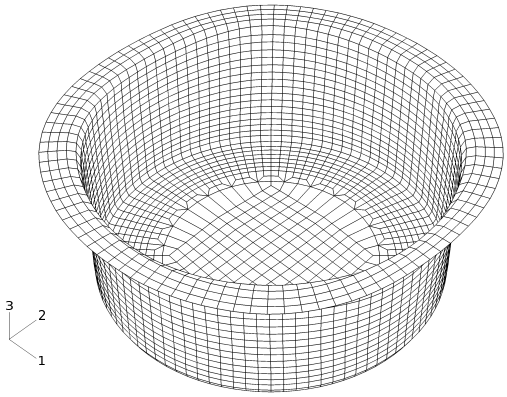

Figure 15: Predicted tinplate steel food can obtained with ABAQUS/Explicit using Hill's quadratic yield criterion and reduced integration shell elements.

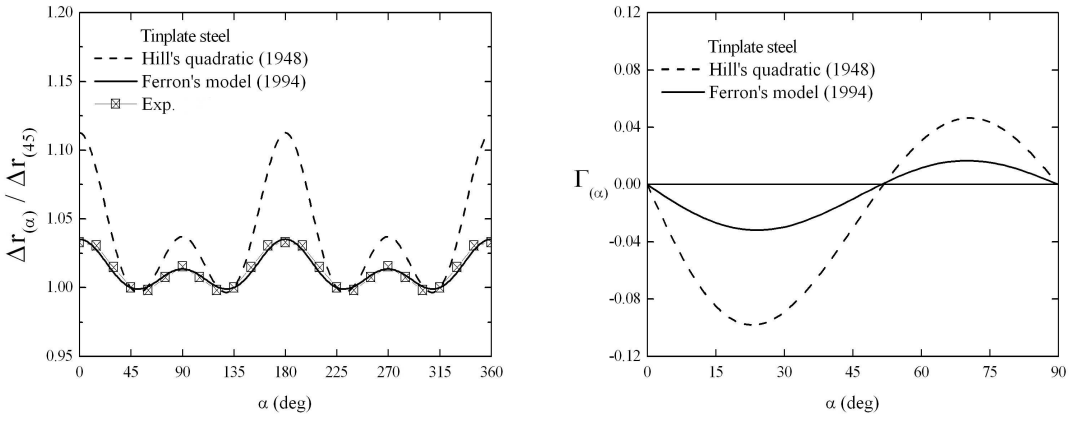

(a) (b)

Figure 16: Earing formation in the deep-drawing of a tinplate steel food can: (a) comparison between the measured normalised flange profile and the predictions obtained using the simplified model proposed by Panchanadeeswaran et al. [3] and (b) angular evolution of the parameter $\Gamma_{(\alpha)}$ introduced by Barlat and Richmond [10].

6 Conclusions

The implementation procedures used with the Fortran user material subroutines UMAT and VUMAT, available in the commercial finite element code ABAQUS, were firstly detailed for either the plane-stress and general 3D stress states in the case of an isotropic linear elastic material under the assumption of an isotropic work-hardening. Afterwards, the parametric description of orthotropic plasticity in metal sheets under plane-stress conditions proposed by Ferron et al. [8] is firstly presented and then extended to the 3D general case. The numerical predictions obtained from the simulations of typical sheet metal forming experiments, namely, the hemispherical punch stretching and the cup-drawing, have shown the good consistency of the implementation of Ferron's model in either implicit and explicit integration techniques available in the ABAQUS code. Also, it has been verified that the response of the plastically deformed sheet closely depends upon the yield stress levels in the different regions of the blank. In all cases analyzed in this work, the strength aspects, i.e., the yield surface shape, are much more important than the kinematic aspects of plastic yielding as measured, for instance, by the anisotropy or Lankford coefficient R. In the hemispherical punch stretching and cup-drawing experiments, the simple assumption of isotropic work-hardening seems to be sufficient to achieve a good agreement with the experimental data, provided a yield function giving an accurate description of the yield or flow stress levels for the stress states of interest is used in the numerical simulations. This observation holds true for either the radial strains distributions or the earing formation in the hemispherical punch stretching and cup-drawing sheet metal forming experiments respectively.

Acknowledgements: LPM is grateful to the "Fundação de Amparo à Pesquisa do Estado do Rio de Janeiro" (FAPERJ) for the research grant APQ1 No. E 26/170.566/2004.

References

[1] B. Bacroix and P. Gilormini. Finite-element simulations of earing in polycrytalline materials using a texture-adjusted strain-rate potential. *Modelling and Simulation in Materials Science and Engineering*, 3:1–21, 1995.

[2] F. Barlat. Crystallographic texture, anisotropic yield surfaces and forming limits of sheet metals. *Materials Science and Engineering A*, 91:55–72, 1987.

[3] F. Barlat and O. Richmond. Prediction of tricomponent plane stress yield surfaces and associated flow and failure behavior of strongly textured f.c.c polycrystalline sheets. *Materials Science and Engineering A*, 95:15–29, 1987.

[4] A.J. Beaudoin, P.R. Dawson, K.K. Mathur, U.F. Kocks, D.A., and Korzekwa. Application of polycrystal plasticity to sheet forming. *Computer Methods in Applied Mechanics and Engineering*, 117:49–70, 1994.

[5] L. Bourne and R. Hill. On the correlation of the directional properties of rolled sheets in tension and cupping tests. *Philosophical Magazine*, 41:671–681, 1950.

[6] D. A. Burford, K. Narasimhan, and R.H. Wagoner. A theoretical sensitivity analysis of full-dome formability tests : parameter study for n, m, r and μ. *Metallurgical Transactions*, 22A:1775–1788, 1991.

[7] D.C. Drucker. Relation of experiments to mathematical theories of plasticity. *Journal of Applied Mechanics, Transactions of the ASME*, 16:349–360, 1949.

[8] G. Ferron, R. Makkouk, and J. Morreale. A parametric description of orthotropic plasticity in metal sheets. *International Journal of Plasticity*, 10:431–449, 1994.

[9] P. Gilormini and Ph. Roudier. Abaqus and finite strain. Technical report lmt n, Laboratoire de Mécanique et Technologie, Université de Paris VI, France, 1993.

[10] R. Hill. A theory of the yielding and plastic flow of anisotropic metals. *Proceedings of the Royal Society of London*, A193:281–297, 1948.

[11] R. Hill. Theoretical plasticity of textured aggregates. *Mathematical Proceedings of the Cambridge Philosophical Society*, 85:179–191, 1979.

[12] J.R. Knibloe and R.H. Wagoner. Experimental investigation and finite element modeling of hemispherically stretched steel sheet. *Metallurgical Transactions*, 10A:1509–1521, 1989.

[13] R.D. Krieg and S.W. Key. Implementation of a time independent plasticity theory into structural computer programs. *Constitutive Equations in Viscoplasticity: Computational and Engineering Aspects, ASME*, 20:125–137, 1976.

[14] L.P. Moreira. *Étude numérique de l'influence du modle de plasticité sur le comportement plastique des tôles minces lors de l'emboutissage.* Thèse de doctorat, Universit de Mez, France, 2002.

[15] L.P. Moreira, G. Ferron, and G. Ferran. Experimental and numerical analysis of the cup drawing test for orthotropic metal sheets. *Journal of Materials Processing Technology*, 108:78–86, 2000.

[16] S. Panchanadeeswaran, O. Richmond, W. G. Fricke, and L. A. Lalli. The effect of texture on earing in cup drawing of rolled high purity aluminum sheets. In *Eighth International Conference on Textures of Materials ICOTOM*, pages 1103–1110, 1988.

[17] Pawtucket. *ABAQUS Theory Manual Version 6.6.* ABAQUS Inc., Rhode Island, USA, 2006.

[18] J. C. Simo and R. L. Taylor. Consistent tangent operators for rate-independent elastoplasticity. *Computer Methods in Applied Mechanics and Engineering*, 48:101–118, 1985.